1-10-2013

Neutron single-particle strength outside the N=50 core

D. K. Sharp
The University of Manchester

B. P. Kay
Argonne National Laboratory

J. S. Thomas
The University of Manchester

S. J. Freeman
The University of Manchester

J. P. Schiffer
Argonne National Laboratory

See next page for additional authors

PHYSICAL REVIEW C **87**, 014312 (2013)

Neutron single-particle strength outside the $N = 50$ core

D. K. Sharp,[1,*] B. P. Kay,[2,†] J. S. Thomas,[1] S. J. Freeman,[1,‡] J. P. Schiffer,[2] B. B. Back,[2] S. Bedoor,[3] T. Bloxham,[4] J. A. Clark,[2] C. M. Deibel,[2,5,§] C. R. Hoffman,[2] A. M. Howard,[1,‖] J. C. Lighthall,[2,3] S. T. Marley,[2,3] A. J. Mitchell,[1] T. Otsuka,[6] P. D. Parker,[7] K. E. Rehm,[2] D. V. Shetty,[3] and A. H. Wuosmaa[3]

[1]*School of Physics and Astronomy, The University of Manchester, Manchester M13 9PL, United Kingdom*
[2]*Argonne National Laboratory, Physics Division, Argonne, Illinois 60439, USA*
[3]*Physics Department, Western Michigan University, Kalamazoo, Michigan 49008, USA*
[4]*Lawrence Berkeley National Laboratory, Berkeley, California 94720, USA*
[5]*Joint Institute for Nuclear Astrophysics, Michigan State University, East Lansing, Michigan 48824, USA*
[6]*Department of Physics, University of Tokyo, Hongo, Bunjyo-ku, Tokyo 113-0033, Japan*
[7]*Yale University, New Haven, Connecticut 06520, USA*

(Received 9 November 2012; published 10 January 2013)

The single-neutron properties of $N = 51$ nuclei have been studied with the (d,p) and $(\alpha,{}^3\mathrm{He})$ reactions, at beam energies of 15 and 50 MeV respectively, on ^{88}Sr, ^{90}Zr, and ^{92}Mo targets. The light reaction products were momentum analyzed using a conventional magnetic spectrometer. Additionally, the $^2\mathrm{H}(^{86}\mathrm{Kr},p)$ reaction was measured at a beam energy of 10 MeV/u, where outgoing light ions were analyzed using a helical-orbit spectrometer. Absolute cross sections and angular distributions corresponding to the population of different final states in the heavy product were obtained for each reaction. Spectroscopic factors were extracted and centroids of the single-particle strength were deduced. The observations appear consistent with calculations based on an evolution of single-particle structure driven by the nucleon-nucleon forces acting between valence protons and neutrons.

DOI: 10.1103/PhysRevC.87.014312 PACS number(s): 21.10.Jx, 21.10.Pc, 25.45.Hi, 25.55.Hp

I. INTRODUCTION

Single-particle phenomena provide much of the underlying framework for our understanding of the structure of atomic nuclei. Recent investigations into the structure of light nuclei have indicated dramatic changes in shell structure away from stability. The ordering of single-particle levels has been found to evolve as a function of proton-neutron ratio and even the locations of the gaps in levels that correspond to shell closures are found to alter. For example, the disappearance of the $N = 20$ magic number, and the emergence of a new shell gap at $N = 16$, have been observed in nuclei near the neutron drip line [1]. These findings have attracted a lot of experimental and theoretical attention in recent years and we have undertaken a careful reinvestigation of the trends of single-particle states in *stable* nuclei, particularly where extensive chains of isotones or isotopes are available, to help understand the underlying causes of such shell evolution.

Recent experimental work on the Sb isotopes [2] and $N = 83$ isotones [3,4] found systematic shifts in the energies of high-j orbitals with changing neutron excess that were difficult to understand. Theoretical approaches have attributed the driving force behind such observed changes to interactions between valence protons and neutrons. The changing occupancy of orbitals corresponding to one type of nucleon, as one moves through a sequence of isotopes or isotones, alters the overall effect of interactions on a nucleon of the other type, thus shifting its effective single-particle energy. In order to properly reproduce the observed trends, it has been found necessary to include the tensor component of the nucleon-nucleon interaction [5,6], in addition to the effects of central forces.

The effect of the tensor interaction between two nucleons depends in part on whether the nucleon orbitals involved correspond to $j_> = \ell + 1/2$ or $j_< = \ell - 1/2$. Combined with the effect of the central terms of the nuclear force, the tensor interaction between neutrons filling the $h_{11/2}$ orbital and valence protons was key to reproducing the observed change in energy of the $\pi g_{7/2}$ and $\pi h_{11/2}$ orbitals across $Z = 51$ nuclei [5]. The effect of the tensor interaction is attractive between $j_>$ and $j_<$ orbitals, such as $\nu h_{11/2}$ and $\pi g_{7/2}$ orbitals, but repulsive between two $j_>$ (or $j_<$) states, as in the case of $\nu h_{11/2}$ and $\pi h_{11/2}$. The escalating effect of this tensor interaction as the $\nu h_{11/2}$ fills is responsible for increasing the separation of these two proton orbitals in energy across Sb isotopes from $A = 113$ to 125 [2]. Similarly, results of a study of neutron states in $N = 83$ isotones have been understood in terms of the changing occupancy of valence proton orbitals that alters the net interactions with neutrons giving rise to the relative changes observed in the $\nu h_{9/2}$ and $\nu i_{13/2}$ orbitals with Z [3,4].

The motivation for the current measurements was to extend these studies to the evolution of single-neutron energies in $N = 51$ nuclei, using the neutron-adding reactions on ^{86}Kr, ^{88}Sr,

*Current address: Smiths Detection Watford Ltd., 459 Park Avenue, Watford, WD23 2BW, United Kingdom.
†Current address: Physics Department, University of York, Heslington, York YO10 5DD, United Kingdom.
‡Correspondence to sean.freeman@manchester.ac.uk
§Current address: Department of Physics and Astronomy, Louisiana State University, Baton Rouge, LA 70803, USA.
‖Current address: Department of Physics, University of Notre Dame, Notre Dame, IN 46556, USA.

^{90}Zr, and ^{92}Mo. With increasing mass across these isotones, the proton Fermi surface moves from the fp shell, dominated by $j_<$ states, to the $j_>$ $g_{9/2}$ orbital. The sense of the tensor interaction with individual neutron states should change at this point, with the expectation that the tensor-driven component to the trends should reverse. Of particular interest are the high-j $\nu g_{7/2}$ and $\nu h_{11/2}$ single-particle orbitals, where the effect of the tensor interaction might be largest.

The (d,p) reaction on $N = 50$ targets has been studied previously [7–18]. However, different experimental techniques and beam energies have been used for each target. The reaction modeling has been performed using many different computer codes, multifarious optical-model sets, and by applying varying approximations. Indeed, in some cases only graphs of relative angular distributions and tables of spectroscopic factors were published; raw cross section data are not always available. Neither the precision nor the consistency that are needed to make quantitative comparisons of data on different nuclei are readily available from the published literature. In addition, the $(\alpha,^3\mathrm{He})$ reaction, preferable for high ℓ transfers to ensure good momentum matching, has only been performed on ^{92}Mo [18] and ^{90}Zr [19] and the resulting data are rather limited. Previous $^2\mathrm{H}(^{86}\mathrm{Kr},p)$ measurements have been performed using gas-cell targets at 5.5 MeV/u [20] and 7.5 MeV/u [21].

Here we report on a study of both the $(\alpha,^3\mathrm{He})$ and (d,p) reactions on the stable solid $N = 50$ isotopes performed using a consistent experimental method employing a conventional magnetic spectrometer. We also have performed a high-resolution inverse-kinematics measurement of the $^2\mathrm{H}(^{86}\mathrm{Kr},p)$ reaction, which avoids the complications of gas-cell windows, using a helical orbit spectrometer [22,23]. Targets are currently not available to perform the $(\alpha,^3\mathrm{He})$ reaction in the same way, so the (d,p) measurement was made at 10 MeV/u, higher than previous studies, to improve the cross sections to high-ℓ states. By adopting, where possible, consistent approaches to the experimental techniques and to the analysis, systematic problems associated with comparing results across all targets can be minimized.

II. REACTIONS ON ^{88}Sr, ^{90}Zr AND ^{92}Mo

Beams of 15-MeV deuterons and 50-MeV α particles were supplied by the Yale tandem Van de Graaf accelerator. They were used to bombard ^{88}Sr, ^{90}Zr, and ^{92}Mo targets with thicknesses 182, 328, and 306 μg/cm^2, respectively. The ^{90}Zr and ^{92}Mo targets were rolled self-supporting foils, whilst the ^{88}Sr target was in oxide form evaporated onto a 20–40 μg/cm^2 carbon foil. All the targets were >98% isotopically enriched, but carbon and oxygen contaminants complicated the analysis, as discussed below.

The light reaction products were momentum analyzed using the Yale Enge split-pole spectrometer. At the focal plane of the spectrograph, a position-sensitive gas-filled ionization chamber was used to measure the position of ions traversing the focal plane. The energy-loss characteristics of ions in the gas detector, and in a plastic scintillator placed behind it, allowed the separation of the protons and ^{3}He ions of interest from other reaction products. The beam current was measured on a tantalum strip at 0° behind the target ladder using a Brookhaven current integrator; the strip and target ladder were biased to prevent escape of electrons. The beam currents used were in the range 30–60 enA. The spectrometer entrance aperture was kept fixed to a nominal value of 2.8 msr throughout the entire experiment to minimize systematic uncertainties.

In order to extract absolute cross sections, the product of target thickness and spectrometer entrance aperture was calibrated using elastic scattering of α particles. This measurement was carried out at a beam energy of 15 MeV and at an angle of 20°. Under these conditions the elastic-scattering cross section is expected to be within 5% of Rutherford scattering according to optical-model calculations using the potentials discussed below. The uncertainty in the cross sections deduced using this method was estimated to be ∼5%. (The target thicknesses quoted above were extracted from this calibration.)

Typical focal-plane spectra are shown in Fig. 1, calibrated in terms of excitation energy in the residual nucleus, using the energy of previously observed states compiled in Refs. [24–26]. The excitation energies with this calibration are estimated to be accurate to better than ∼5 keV. The energy resolution observed for the (d,p) reaction was ∼45 keV and ∼80 keV for the $(\alpha,^3\mathrm{He})$ reaction. Ions from reactions on ^{12}C and ^{16}O target contaminants appear as peaks in the spectra with larger widths compared to the groups of interest due to the higher kinematic shift associated with the lower masses. At particular angles, the contaminant peaks obscure some of the peaks of interest. However, the difference in kinematic shift can be harnessed to move contaminant groups away from obscured peaks by a change in the spectrometer angle.

The choice of angles was largely dictated by the desire to extract spectroscopic factors near the first maximum in the angular distributions, where approximations associated with the distorted wave Born approximation (DWBA), used for reaction modeling, are best met. The resulting set of angles also maps out angular distributions sufficiently to discriminate between different values of orbital angular momentum transfer, ℓ. The (d,p) reaction was measured at laboratory angles of 18°, 34°, and 42°, corresponding to the first maxima in the angular distributions associated with $\ell = 2$, 4, and 5, respectively. Measurements were also made as far forward in laboratory angle as possible; the closest angle to the zero-degree peak for $\ell = 0$ transitions that could be used was 7°. The shift of the contaminant peaks was such that (d,p) cross sections could be extracted for at least two angles for all observed states in this reaction. The angular distributions for the $(\alpha,^3\mathrm{He})$ reaction tend to be forward peaked for all angular momentum transfers, so measurements were made at 5° for all targets. Contamination was a problem for the ^{88}Sr and ^{90}Zr targets, so additional angles of 10° and 22.5° were used for the α-induced reaction to reveal all states for at least one angle.

Angular-momentum assignments for the majority of the states populated have been made in previous work [7–19]; these were checked using measured angular distributions and information gained by a comparison of cross sections from the two different reactions used.

The measured angular distributions are shown in Figs. 2, 3 and 4, where the data are compared with results of finite-range

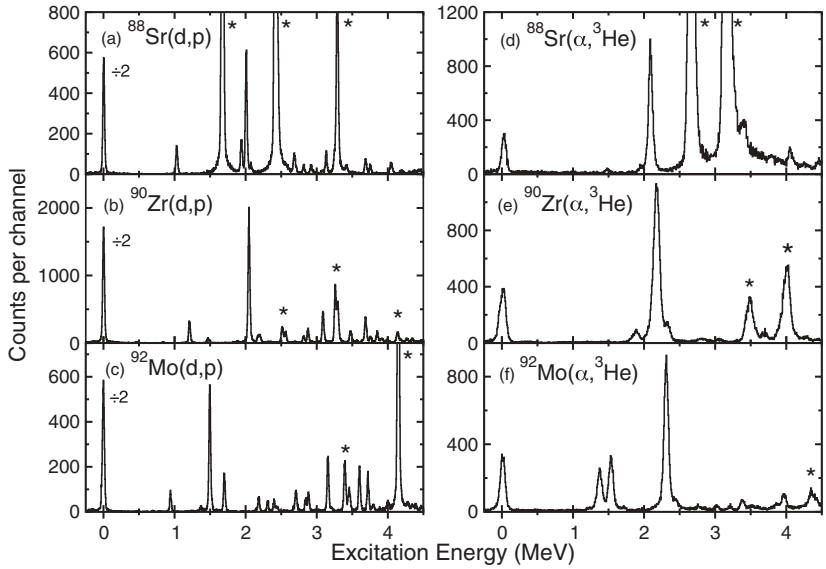

FIG. 1. (a)–(c) Spectra for protons from the (d,p) reaction on targets of ^{88}Sr, ^{90}Zr, and ^{92}Mo respectively at 18°, displayed in terms of the excitation energy in the residual nucleus. (d)–(f) Similar spectra for outgoing ^{3}He ions in the $(\alpha,^3\mathrm{He})$ reactions at 5° for the same targets. The ground-state transition has been scaled down by a factor of two where indicated. Peaks marked with an asterisk arise from reactions on light target contaminants.

DWBA calculations for the assigned ℓ value, performed using the computer code PTOLEMY [27]. Optical-model parameters were taken from Refs. [28] and [29] to describe the α and ^{3}He channels, while global sets from Refs. [30] and [31] were used for deuterons and protons, respectively. A Reid potential was used to generate the internal wave function for the deuteron [32]. Other bound states were calculated using a Woods-Saxon potential whose depth was fitted to the measured binding energies. Bound-state parameters for a neutron in the α-particle projectile ($r = 1.20$ fm and $a = 0.65$ fm) were taken from Ref. [33]; those for a neutron bound to the target ($r = 1.25$ fm, $a = 0.63$ fm, $V_{so} = 7$ MeV, $r_{so} = 1.10$ fm and $a_{so} = 0.50$ fm) were from Ref. [34]. A range of other potential sets [35–40] were also investigated with little change in the shape of the calculated distributions.

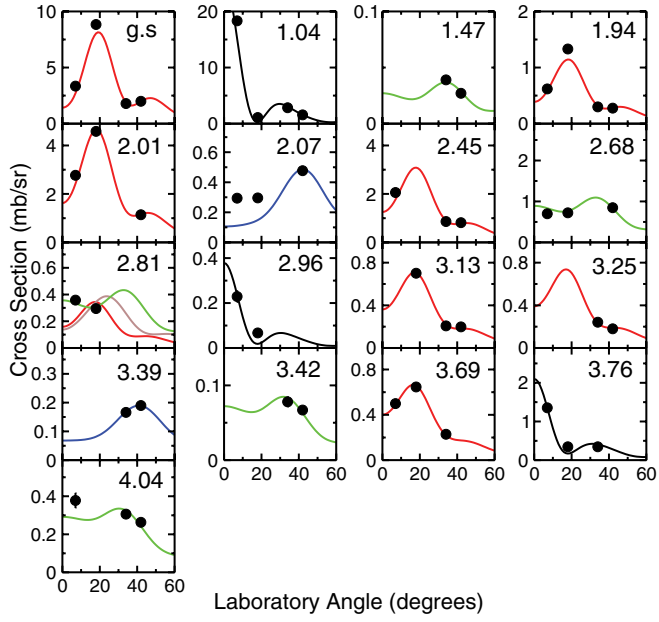

FIG. 2. (Color online) Angular distributions for outgoing protons in the (d,p) reactions on ^{88}Sr. The solid curves are DWBA calculations, normalized to the data, based on the assigned ℓ values given in Table I (black: $\ell = 0$; red: $\ell = 2$; brown: $\ell = 3$; green: $\ell = 4$; and blue: $\ell = 5$ in the online version). For the state at 2.814 MeV, in the absence of a firm assignment, calculations are shown for $\ell = 2$, 3, and 4. Excited states are labeled by their energy in MeV.

Different momentum matching in the (d,p) and $(\alpha,^3\mathrm{He})$ reactions lends ℓ sensitivity to the ratio of cross sections in the two reactions to the same final state. This is illustrated in Fig. 5, where the ratio is plotted as a function of excitation energy and compared to DWBA predictions that were scaled onto a data point for a strong state of known ℓ value. Data points arising from different ℓ values are clearly separated along trajectories that correspond well to the predicted Q-value dependence. In order to check assignments for all observed states, different combinations of angles were used since, at some angles, particular states in ^{91}Zr and ^{89}Sr were obscured by contaminants. Not all transitions could be investigated in this way as some of the weaker states are not clearly observed in both reactions; $\ell = 0$ states, for example, are not strongly populated in the $(\alpha,^3\mathrm{He})$ reaction, but their distinctive forward peaked distributions are sufficient for current purposes.

Spin-parity assignments were taken from previous work [24–26] and informed by the assumption that only single-particle states in the $N = 50$–82 shell would be populated strongly, corresponding to the $2s_{1/2}$, $1d_{5/2}$, $1d_{3/2}$, $0g_{7/2}$, and $0h_{11/2}$ orbitals. A summary of the assignments, peak cross sections and spectroscopic factors (normalized using the prescription described in Sec. IV below) is given in Tables I, II, and III. Some weak population of states via $\ell = 1$ and 3 transfer was observed, which has previously been attributed to incomplete filling of the fp shell, for example in Ref. [9].

The measured angular distributions and reaction ratios generally agree well with assignments found in evaluated compilations of the literature [24–26]. A small number of previously unobserved states and changes to assignments are discussed briefly here.

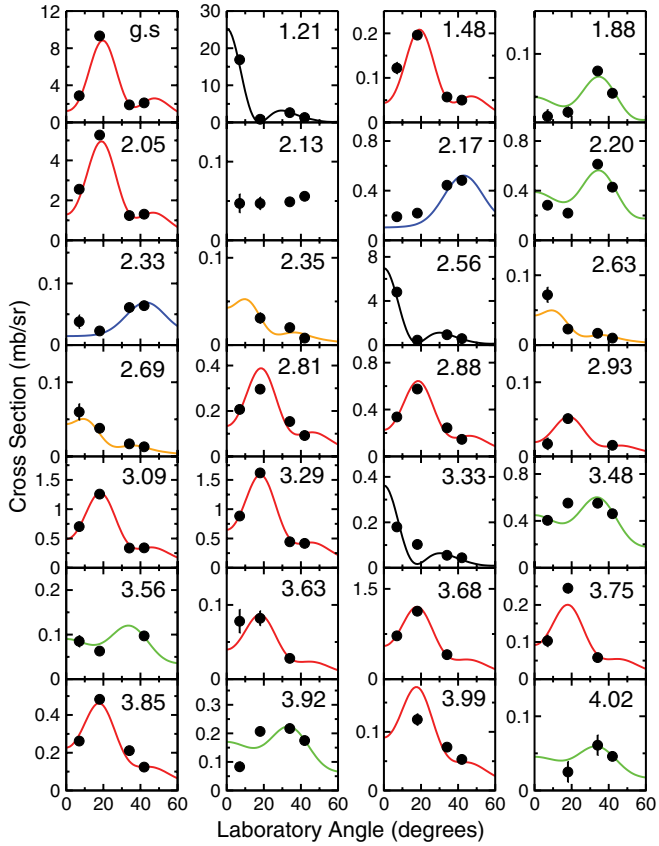

FIG. 3. (Color online) Angular distributions for outgoing protons in the (d,p) reactions on ^{90}Zr. The solid curves are DWBA calculations, normalized to the data, based on the assigned ℓ values given in Table II (black: $\ell = 0$; orange: $\ell = 1$; red: $\ell = 2$; brown: $\ell = 3$; green: $\ell = 4$; and blue: $\ell = 5$ in the online version). For the 2.131-MeV transition, no ℓ value, consistent with the nonobservation in the $(\alpha,^3\mathrm{He})$ reaction, gives a reasonable reproduction of this weak state. Excited states are labeled by their energy in MeV.

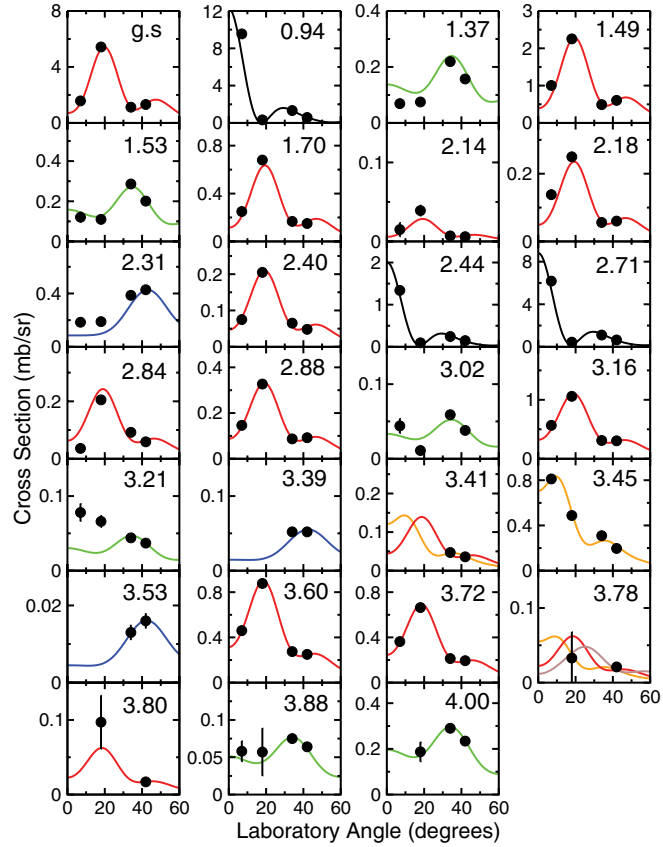

FIG. 4. (Color online) Angular distributions for outgoing protons in the (d,p) reactions on ^{92}Mo. The solid curves are DWBA calculations, normalized to the data, based on the assigned ℓ values given in Table III (black: $\ell = 0$; orange: $\ell = 1$; red: $\ell = 2$; brown: $\ell = 3$; green: $\ell = 4$; and blue: $\ell = 5$ in the online version). In the absence of firm assignments, for the state at 3.412 MeV calculations are shown for $\ell = 2, 3$ and for the state at 3.778 MeV calculations are shown for $\ell = 1, 2, 3$. Excited states are labeled by their energy in MeV.

In ^{89}Sr, assigned $\ell = 0$ and 4 transfers populate states at 2.961 and 4.042 MeV which do not appear to correspond to previously observed states to within the estimated errors of ∼5 keV. The angular distribution and reaction ratio for the transition to the state at 3.42 MeV point to an $\ell = 4$ assignment; a previous study [10] assigned this as $\ell = 5$ on the basis of angular distributions at backward angles. In ^{91}Zr, it is difficult to connect states populated at 2.625, 2.690, 2.813, and 3.917 MeV to previously observed states at similar excitation energies. The state at 2.131 MeV is also populated in an $\ell = 4$ transition in the ^{92}Zr(p,d) reaction [9] and this state has a previous $9/2^+$ attribution that was based on evidence from $(n, n'\gamma)$ excitation functions [41]. In the current work, the population in the (d,p) reaction is weak, the angular distribution is inconclusive and it is not observed in the $(\alpha,^3\mathrm{He})$ reaction. This may indicate the observed population is via a nondirect process. In ^{93}Mo, the $\ell = 2$ transitions at 2.838, 2.876, and 3.797 MeV are difficult to match to previously observed transitions, as are the states at 3.412 and 3.778 MeV for which the current angular distributions are not conclusive. The $(\alpha,^3\mathrm{He})$ reaction has also revealed a few new high-ℓ transitions.

There are a small number of transitions seen in the current work up to ∼4 MeV where assignments have not been possible; these are weakly populated states whose spectroscopic factors are at the 1% level, or less, for any plausible ℓ assignment.

III. REACTIONS ON ^{86}Kr

The ^{2}H$(^{86}\mathrm{Kr}, p)^{87}$Kr measurement was performed in inverse kinematics to avoid the difficulties associated with using a gas target. A 10-MeV/u beam of ^{86}Kr was delivered by the Argonne Tandem-Linac Accelerator System (ATLAS) and used to bombard a deuterated polyethylene $(C_2D_4)_n$ target. Thin targets were used in this experiment, with nominal thicknesses between 50–75 μg/cm^2, to minimize the contribution to the energy resolution of the outgoing light ions due to energy losses in the target. The beam intensity was limited to $\sim 5 \times 10^7$ ions per second in order to extend the useful lifetime of the targets.

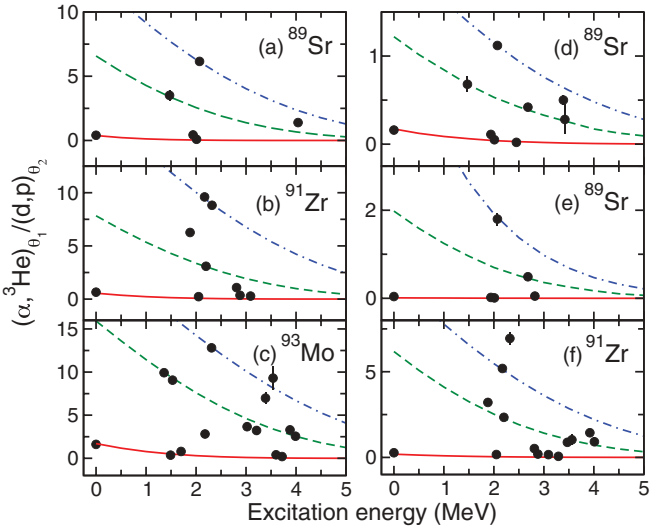

FIG. 5. (Color online) Ratios of cross sections in the (α,^{3}He) reaction at an angle θ_1 and the (d,p) reaction at an angle θ_2 labeled by the residual nucleus: (a) ^{88}Sr target for $\theta_1 = 5^\circ$ and $\theta_2 = 42^\circ$, (b) ^{90}Zr target with the same angle combination, (c) ^{92}Mo target with the same angle combination, (d) ^{88}Sr target for $\theta_1 = 22.5^\circ$ and $\theta_2 = 42^\circ$, (e) ^{88}Sr target for $\theta_1 = 22.5^\circ$ and $\theta_2 = 18^\circ$, and (f) ^{90}Zr target for $\theta_1 = 10^\circ$ and $\theta_2 = 42^\circ$. The lines are the results of DWBA calculations for $\ell = 2$ (red solid line), $\ell = 4$ (green dashed line) and $\ell = 5$ (blue dash-dotted line) that have been normalized to the ratio for a strong state with known ℓ value.

TABLE I. Summary of states populated in ^{89}Sr via the (d,p) and (α,^{3}He) reactions. Assigned ℓ, J^π and deduced values of C^2S are given. The cross sections are quoted for $\ell = 0$ and 2 transfers from the (d,p) data, and for $\ell = 4$ and 5 from the (α,^{3}He) reaction, at the angle specified. J^π assignments are taken from Ref. [24]. Spectroscopic factors have been normalized according to the procedure described in Sec. IV. The excitation energies are quoted from the current measurements with an estimated uncertainty of ∼5 keV.

E_x (MeV)	ℓ	J^π	$\sigma(\theta)$ (mb/sr)	θ	C^2S
0	2	$5/2^+$	8.8(1)	18°	0.86
1.037	0	$1/2^+$	18.3(1)	7°	0.86
1.468	4	$7/2^+$	0.093(8)	5°	0.021
1.942	2	$5/2^+$	1.33(4)	18°	0.094
2.008	2	$3/2^+$	4.58(7)	18°	0.46
2.069	5	$11/2^-$	2.94(4)	5°	0.27
2.449	2	$3/2^+$	0.86(1)	34°	0.32
2.684	4	$7/2^+$	0.354(7)	22.5°	0.64
2.814			0.29(2)	18°	
2.961	0	$1/2^+$	0.23(3)	7°	0.013
3.132	2	$3/2^+$	0.70(3)	18°	0.058
3.251	2	$5/2^+$	0.242(6)	18°	0.043
3.392	5	$11/2^-$	0.10(1)	22.5°	0.064
3.420	4	$7/2^+$	0.02(1)	22.5°	0.043
3.692	2	$5/2^+$	0.65(3)	18°	0.034
3.761	0	$1/2^+$	1.352(1)	7°	0.093
4.042	4	$7/2^+$	0.37(1)	5°	0.25

Out-going light ions were analyzed using the Helical-Orbit Spectrometer (HELIOS) [22,23]. HELIOS consists of a superconducting solenoidal magnet with its axis along the beam direction. It is 2.35 m in length with a bore of 0.9 m and a central field set at 2 T for the purposes of this experiment. The angular distributions of protons from the (d,p) reaction are forward peaked in the center-of-mass frame, but appear in the laboratory frame in the backwards hemisphere with $\theta_{\rm lab} > 90^\circ$. In the uniform field of HELIOS, ions emitted from the target position follow helical orbits, returning to the magnetic axis after one cyclotron period. They are detected using an array of 24 position-sensitive Si detectors, arranged in rings of four around the axis in a box configuration. Six rings of detectors were mounted, although only 19 individual detectors were operational in this experiment. These were calibrated using ^{148}Gd and ^{228}Th α-particle sources placed at the target position. The target was positioned at a distance 30 cm downstream from the nearest edge of the Si array, as shown in Fig. 6. The silicon detectors measure the ion energy, the position along the axis, and the time of flight relative to the radio frequency of the ATLAS accelerator. The time of flight corresponds to the cyclotron frequency, which is used to identify the ion species. Other parameters of interest can be obtained by combining the cyclotron frequency with the measured energy and the distance from the target at which the ions return to the axis Δz, as described in detail in Refs. [22,23].

In order to extract absolute cross sections the product of the beam intensity and the areal density of deuterons in the target was measured throughout the experiment. A Si surface-barrier detector was positioned at a distance of 360 mm downstream from the target (see Fig. 6) such that elastically scattered deuterons are intercepted at an angle corresponding to 29° in the center-of-mass frame. The beam dose was found by integrating the charge collected by a Faraday cup positioned in front of the surface barrier detector. Under these conditions, the deuteron elastic scattering cross section is approximately 50% of the Rutherford-scattering cross section; the absolute cross section used to deduce the target thickness was obtained by performing optical-model calculations using the parameter set from Ref. [30].

Events corresponding to protons that have executed one orbit were clearly identified by their time of flight, corresponding to a cyclotron period of 32.8 ns. A timing resolution of ∼7 ns FWHM was obtained. A representative time spectrum is shown in Fig. 7, where a second peak at 65.6 ns is also visible. This corresponds to both α particles and a fraction of events where protons perform two cyclotron orbits by crossing the beam axis in the space between target and the end of the array.

The array covered center-of-mass angles from around 10° to 40°, the exact range of angles depending on the excitation energy of the state. Each individual silicon detector corresponds to an angular bin with equal solid angle coverage in the center-of-mass frame. Yields from the α-particle source calibration were used to correct for efficiency differences between the detectors. The angular distributions were formed using data from each ring of silicon detectors, plotted at the center-of-mass angle corresponding to the middle of the

TABLE II. Summary of states populated in ^{91}Zr via the (d,p) and $(\alpha,^3\mathrm{He})$ reactions. Assigned ℓ, J^π and deduced values of C^2S are given. The cross sections are quoted for $\ell = 0$ and 2 transfers from the (d,p) data, and for $\ell = 4$ and 5 from the $(\alpha,^3\mathrm{He})$ reaction, at the angle specified in the table. J^π assignments are taken from Ref. [25]. Spectroscopic factors have been normalized according to the procedure described in Sec. IV. For $\ell = 2$ transitions without a firm J^π assignment, values of spectroscopic factors are quoted for $J^\pi = 3/2^+$(see text for details). The excitation energies are quoted from the current measurements with an estimated uncertainty of ∼5 keV.

E_x (MeV)	ℓ	J^π	$\sigma(\theta)$ (mb/sr)	θ	C^2S
0	2	$5/2^+$	9.35(6)	18°	1.05
1.212	0	$1/2^+$	17.0(1)	7°	0.83
1.476	2	$5/2^+$	0.197(9)	18°	0.018
1.877	4	$7/2^+$	0.34(1)	5°	0.078
2.048	2	$3/2^+$	5.29(4)	18°	0.63
2.131			0.049(26)	34°	
2.171	5	$11/2^-$	4.7(1)	5°	0.40
2.203	4	$7/2^+$	1.3(1)	5°	0.34
2.333	5	$11/2^-$	0.55(2)	5°	0.048
2.354	1	$1/2^-, 3/2^-$	0.031(6)	18°	0.004, 0.002
2.559	0	$1/2^+$	4.83(6)	7°	0.24
2.625	1	$1/2^-, 3/2^-$	0.07(1)	7°	0.006, 0.003
2.690	1	$1/2^-, 3/2^-$	0.06(1)	7°	0.005, 0.003
2.813	2	$3/2^+, 5/2^+$	0.30(1)	18°	0.11
2.875	2	$3/2^+$	0.58(1)	18°	0.21
2.928	2	$3/2^+, 5/2^+$	0.051(6)	18°	0.018
3.087	2	$3/2^+$	1.26(2)	18°	0.12
3.291	2	$3/2^+$	1.63(3)	18°	0.15
3.330	0	$1/2^+$	0.18(2)	7°	0.010
3.475	4	$7/2^+$	0.41(2)	10°	0.28
3.558	4	$7/2^+$	0.10(3)	10°	0.072
3.631	2	$3/2^+, 5/2^+$	0.08(1)	18°	0.007
3.682	2	$3/2^+$	1.13(2)	18°	0.10
3.751	2	$3/2^+, 5/2^+$	0.25(1)	18°	0.022
3.850	2	$5/2^+$	0.48(2)	18°	0.019
3.917	4	$7/2^+$	0.25(1)	10°	0.21
3.992	2	$3/2^+, 5/2^+$	0.12(1)	18°	0.010
4.018	4	$7/2^+$	0.04(1)	10°	0.036

TABLE III. Summary of states populated in ^{93}Mo via the (d,p) and $(\alpha,^3\mathrm{He})$ reactions. Assigned ℓ, J^π and deduced values of C^2S are given. The cross sections are quoted for $\ell = 0$ and 2 transfers from the (d,p) data, and for $\ell = 4$ and 5 from the $(\alpha,^3\mathrm{He})$ reaction, at the angle specified in the table. J^π assignments are taken from Ref. [26]. Spectroscopic factors have been normalized according to the procedure described in Sec. IV. For $\ell = 2$ transitions without a firm J^π assignment, values of spectroscopic factors are quoted for $J^\pi = 3/2^+$ (see text for details). The excitation energies are quoted from the current measurements with an estimated uncertainty of ∼5 keV.

E_x (MeV)	ℓ	J^π	$\sigma(\theta)$ (mb/sr)	θ	C^2S
0	2	$5/2^+$	5.44(5)	18°	0.73
0.943	0	$1/2^+$	9.6(1)	7°	0.53
1.365	4	$7/2^+$	1.57(3)	5°	0.27
1.493	2	$3/2^+$	2.26(4)	18°	0.36
1.525	4	$7/2^+$	1.83(4)	5°	0.33
1.698	2	$5/2^+$	0.68(2)	18°	0.073
2.144	2	$5/2^+$	0.039(7)	18°	0.004
2.179	2	$3/2^+$	0.25(1)	18°	0.036
2.311	5	$11/2^-$	5.50(6)	5°	0.45
2.399	2	$5/2^+$	0.21(1)	18°	0.020
2.442	0	$1/2^+$	1.34(4)	7°	0.071
2.705	0	$1/2^+$	6.20(8)	7°	0.33
2.838	2	$3/2^+$	0.21(1)	18°	0.026
2.876	2	$3/2^+, 5/2^+$	0.33(2)	18°	0.042
3.023	4	$7/2^+$	0.14(2)	5°	0.040
3.156	2	$3/2^+, 5/2^+$	1.06(3)	18°	0.13
3.210	4	$7/2^+$	0.12(2)	5°	0.056
3.385	5	$11/2^-$	0.37(2)	5°	0.038
3.412			0.047(5)	34°	
3.448	(1)	$(1/2^-, 3/2^-)$	0.81(3)	7°	0.066, 0.044
3.529	5	$11/2^-$	0.15(1)	5°	0.018
3.598	2	$3/2^+, 5/2^+$	0.88(2)	18°	0.10
3.715	2	$3/2^+, 5/2^+$	0.67(2)	18°	0.073
3.778			0.03(4)	18°	
3.797	2	$3/2^+, 5/2^+$	0.10(4)	18°	0.011
3.880	4	$7/2^+$	0.21(2)	5°	0.085
4.000	4	$7/2^+$	0.60(2)	5°	0.25

ring where the populated state covers the entire range of the detector.

The measured energy is plotted in Fig. 8 against Δz for ions with a time-of-flight corresponding to one proton cyclotron period for one complete row of six detectors. The sloping lines in this plot correspond to the population of different final states in the residual nucleus. A representative excitation spectrum is shown in Fig. 9 for one detector; the variation of proton energy with Δz has been corrected to obtain the best energy resolution. The typical excitation-energy resolution across the array was ∼80 keV, although this varied between detectors in the range 70–160 keV as the dominant contribution arose from the intrinsic response of each detector [23].

Angular distributions for each state populated are shown in Fig. 10, where they are compared to the results of finite-range DWBA calculations performed using the same methodology as in the previous sections. Since only one target-array distance was used, the resulting angular coverage is rather restricted. However, ℓ assignments were taken from previous studies [20, 21], where angular distributions over a greater range of angles were obtained, and the current results shown in Fig. 10 are used as a consistency check.

The angular distributions measured here are generally consistent with the assignments of Ref. [20]. The majority of the observed transfer strength is $\ell = 2$, with single $\ell = 4$ and 5 transitions at excitation energies of 2.52 and 2.25 MeV. The states previously reported at excitation energies of 3.223 and 3.237 MeV could not be separated in the current data. There was some inconsistency in previous work as this doublet had been assigned as two $\ell = 2$ states in Ref. [20] and an $\ell = 0 + 2$ doublet in Ref. [21]. The current angular distribution suggests a dominant $\ell = 0$ strength; a combined fit of $\ell = 0$ and $\ell = 2$ resulted in less than 1% of the $\ell = 2$ strength. Of the other

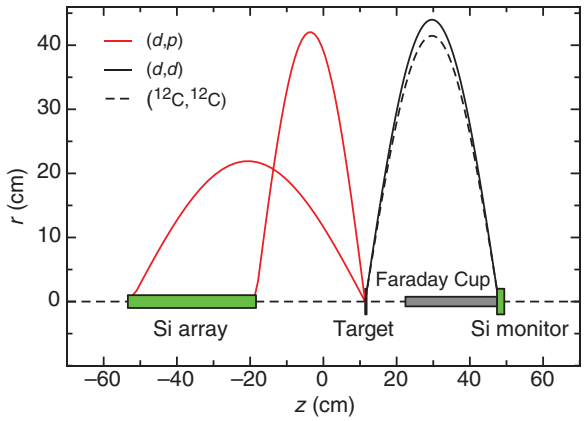

FIG. 6. (Color online) Schematic diagram of the arrangement of the position-sensitive silicon detector array, Faraday cup, target, and Si monitor detector in HELIOS for the ^{2}H(^{86}Kr, p)^{87}Kr measurement. The beam enters from the left of the diagram, along the z axis. The radial distance of an example proton trajectory (red online) is shown as a function of z upstream of the target. The trajectories of elastically scattered ions that are incident on the monitor detector, are also given for scattering of deuterons (black solid line) and ^{12}C (black dashed line) from the target.

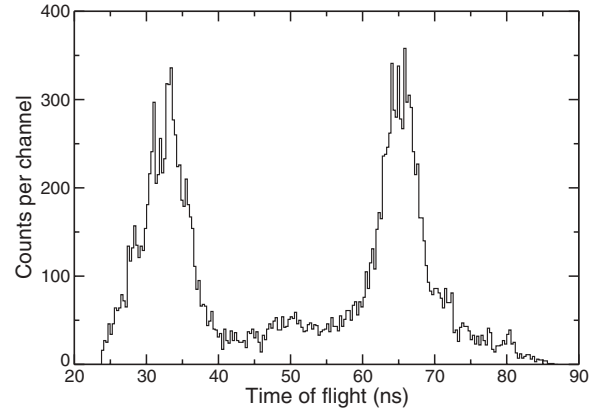

FIG. 7. A typical spectrum of the time of flight of ions between target and one of the detectors in the silicon array, which corresponds to the cyclotron frequency of the ion trajectory in the field of the solenoid (see text for details).

$\ell = 0$ strength populated here, the assignments of the 0.54-, 2.08-, and 2.28-MeV states are taken from Ref. [20]; the angular range of the current data is not optimal for checking $\ell = 0$ transitions, but the angular distributions for these states do not look inconsistent with the previous assignments. Population of the state at 1.57 MeV was observed, but no assignment made, in Ref. [20]. Given that the current angular distribution associated with this level displays some similarity with those for 0.54-, 2.08-, 2.28 and 3.23-MeV states and that expected for an $\ell = 0$ transition, a tentative $\ell = 0$ assignment has been used here. This is not inconsistent with the ($1/2^{+}$, $3/2^{+}$, $5/2^{+}$) spin possibilities obtained from $\beta\gamma$ experiments collated in Ref. [42].

The cross sections deduced from this work are summarized in Table IV. There was no single dominant contribution to estimates of the uncertainty. Important contributions arise from the target-thickness measurement; in particular, those associated with the solid angle of the silicon monitor detector ($\sim$15%) and variation in the elastic scattering cross section for different choices of optical potential ($\sim$10%). These combine with the uncertainties in the array solid angles ($\sim$10%) and the statistical error on the (d,p) yields ($\sim$10%) to give an estimated accuracy of $\sim$25% on the absolute cross section.

IV. DWBA ANALYSIS AND SPECTROSCOPIC FACTORS.

The spectroscopic factors were deduced from the experimental cross sections by comparison with the DWBA calculations. The optical-model potentials and bound-state parameters used in the calculations were summarized above.

In order to best meet the approximations used in the DWBA reaction modeling, data corresponding to the highest direct yield were used for the reactions on ^{88}Sr, ^{90}Zr and ^{92}Mo. The (d,p) reaction was used to determine spectroscopic factors for states populated in low ℓ transfers and the (α,^{3}He) reaction was used for the higher ℓ values. For the majority of transitions, the cross section at angles corresponding to the first maximum of the angular distribution was used. For the (α,^{3}He) reaction, the angular distributions are generally featureless and forward peaked, so the 5° cross sections were used where possible. Where the spectra were obscured by contaminants, data at other angles had to be used; however, it was found that the extracted spectroscopic factors for transitions seen over the full angular range had a variation with angle of typically less than 10%.

The measured angular range for the ^{2}H(^{86}Kr, p)^{87}Kr reaction did not encompass properly the first peak of the distributions; for most states the spectroscopic factors were derived from the whole measured angular range. However, to avoid the issues associated with correctly reproducing minima in the DWBA distributions, for the $\ell = 0$ transitions, data

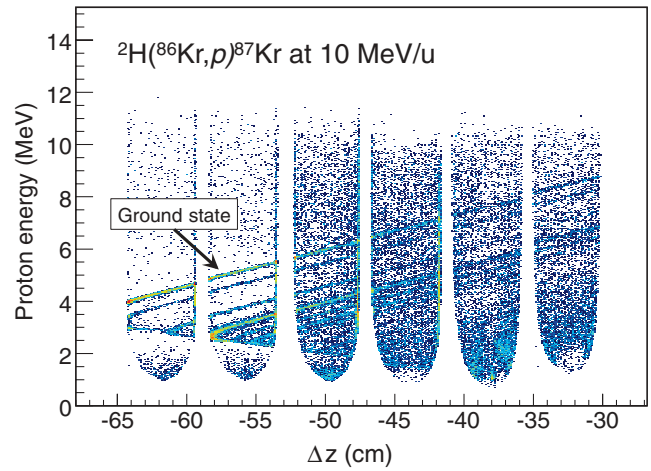

FIG. 8. (Color online) The energy of incident protons plotted against target-to-detector distance Δz for a complete row of detectors for the ^{2}H(^{86}Kr, p)^{87}Kr reaction at 10 MeV/u. A time gate has been applied corresponding to the cyclotron period of a single proton orbit.

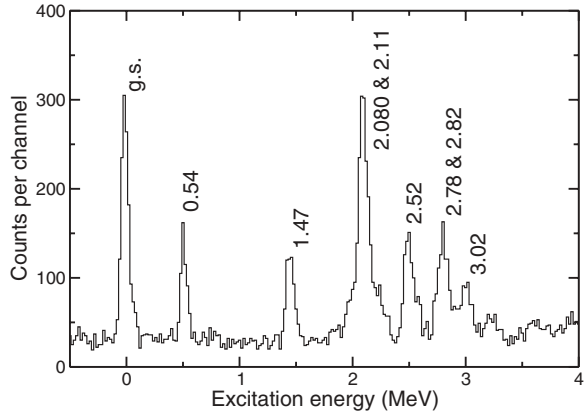

FIG. 9. A representative excitation spectrum of outgoing protons for a single Si detector for the ^{2}H(^{86}Kr, p)^{87}Kr reaction at 10 MeV/u. Some of the prominent peaks are labeled by excitation energy in MeV.

points close to the first minimum were excluded. Although the Kr data were treated differently in this sense, the results did not appear anomalous in the normalization analysis described below.

There is some uncertainty in the absolute normalization of cross sections from DWBA reaction calculations, but it has been shown that consistent results can be obtained by employing a systematic approach to this normalization, see for example Ref. [43]. In the current work, a single common normalization factor for each reaction has been chosen to ensure that the total low-lying summed transfer strength involving a particular single-particle orbital is unity and therefore the Macfarlane-French sum rules [44] are satisfied. While in the final analysis a single normalization value is applied across all targets and all ℓ transfers for a given reaction, the degree to which normalization constants, extracted from

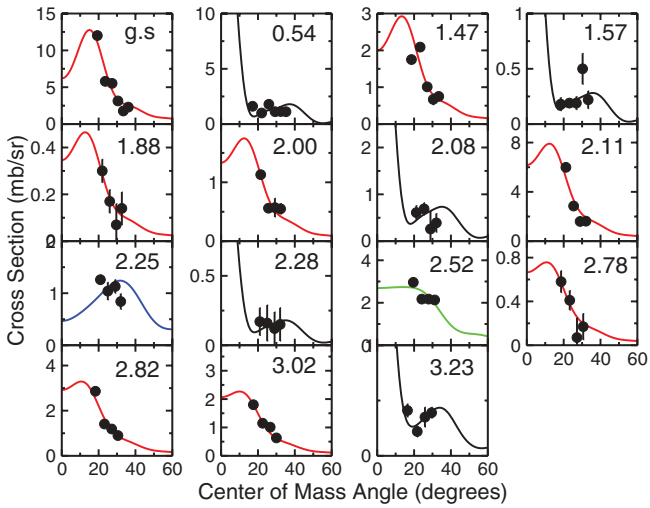

FIG. 10. (Color online) Angular distributions for outgoing protons in the (d,p) reactions on ^{86}Kr. The solid curves are DWBA calculations, normalized to the data, based on the assigned ℓ values given in Table IV (black: $\ell = 0$; red: $\ell = 2$; green: $\ell = 4$; and blue: $\ell = 5$). Excited states are labeled by their energy in MeV.

subsets of the data, are consistent between different ℓ transfers and across different targets is able to give confidence about the extent to which all the low-lying strength has been observed, even where that strength is fragmented. The consistency with analyses of independent data sets is also instructive.

In the (d,p) reaction, the mean $\ell = 0$ normalization factor was found to be 0.63(3) across the targets used. For $\ell = 2$ transitions, there is ambiguity for some states without a definitive J^{π} assignment. However, where firm assignments have been made, it appears that the $d_{5/2}$ strength is largely confined to the ground state. Following this observation, for excited states without firm assignment, $J = 3/2^{+}$ is assumed here. This yields normalization factors of 0.63(3) for $J = 5/2^{+}$ and 0.64(8) for $J = 3/2^{+}$, both consistent with the $\ell = 0$ value.

The (d,p) normalization for $\ell = 4$ transitions is 0.58(4). The spectroscopic factors obtained using this normalization for the weaker $\ell = 4$ transitions in the (d,p) reaction were somewhat inconsistent with those from the better matched $(\alpha,^{3}\mathrm{He})$ reaction, even though there was reasonable agreement for the strongly populated states. For $\ell = 5$, the normalization was considerably lower with a value of 0.35(3), suggesting either that poor matching has consequences or that there is significant unobserved strength.

Based on these considerations, a common single normalization of 0.63(2) was adopted for the (d,p) reaction, corresponding to the weighted average over $\ell = 0$ and 2 transitions.

In the $(\alpha,^{3}\mathrm{He})$ reaction, the $\ell = 4$ normalization is found to be 0.55(1), assuming a projectile spectroscopic factor for neutron removal from ^{4}He to the ^{3}He+n system of ~2.0. It is not unexpected to find a slightly different normalization from the (d,p) results since it is difficult to model two such different reactions in a uniform fashion. The extracted normalization for $\ell = 5$ is approximately half that for $\ell = 4$, with a value of 0.24(3), suggesting strength remains unobserved. Missing $\ell = 5$ strength has also been reported in previous work, for example, in Refs. [10,17]. The $\ell = 4$ normalization is therefore adopted as the common single normalization for the $(\alpha,^{3}\mathrm{He})$ reaction.

In both reactions, the individual contributions to the average normalization from different targets and ℓ values are consistent to within a variation of ~15%.

A number of similar experiments have now been performed by our collaboration and it is instructive to compare normalizations extracted in a similar way to those values deduced here, as summarized in Table V. With similar methods and bombarding energies, and the same optical potentials and bound states, a normalization of 0.58(2) was found for the (p,d) reaction on $N = 82$ targets [45]. By ensuring that the strengths from nucleon-addition and nucleon-removal reactions sum to the orbital degeneracy, a value of 0.64(5) has been found for the (d,p) and (p,d) reactions on the stable Ni isotopes, again using the same optical potentials [43]. These compare very well with the current work and the level of consistency across a wide mass range gives confidence in the method employed and in the value obtained. It is interesting to note that the observation of 50%–60% of the full single-particle strength associated with an orbital over

TABLE IV. Summary of identified states in the ^{2}H(^{86}Kr, p)^{87}Kr reaction with ℓ and J^{π} quantum numbers, and deduced values of $C^{2}S$. The cross section is also given for the particular center-of-mass angle given in the table. Spectroscopic factors have been normalized according to the procedure described in Sec. IV. Uncertainties on the cross sections and spectroscopic factors are discussed in the text. J^{π} and ℓ assignments are taken from Ref. [20,21], apart from the 1.57-MeV state which is discussed in the text. For $\ell = 2$ transitions without a firm J^{π} assignment, values of spectroscopic factors are quoted for $J^{\pi} = 3/2^{+}$ (see text for details). The excitation energies are quoted from the current measurements with an estimated uncertainty of ∼10 keV.

E_x (MeV)	ℓ	J^{π}	$\sigma(\theta)$ (mb/sr)	θ	$C^{2}S$
0	2	$5/2^{+}$	12.01(25)	19.3°	1.02
0.54	0	$1/2^{+}$	1.12(10)	35.2°	0.69
1.47	2	$3/2^{+}$, $5/2^{+}$	1.75(11)	18.6°	0.19
1.57	(0)	$1/2^{+}$	0.22(8)	33.3°	0.17
1.88	2	$3/2^{+}$, $5/2^{+}$	0.30(5)	22.0°	0.030
2.00	2	$3/2^{+}$, $5/2^{+}$	1.13(7)	21.5°	0.11
2.08	0	$1/2^{+}$	0.39(20)	32.1°	0.19
2.11	2	$3/2^{+}$, $5/2^{+}$	5.99(16)	21.2°	0.47
2.25	(5)	$(11/2^{-})$	0.84(15)	32.0°	0.75
2.28	(0)	$1/2^{+}$	0.15(12)	32.0°	0.094
2.52	4	$7/2^{+}$	2.13(10)	31.2°	0.96
2.78	2	$3/2^{+}$, $5/2^{+}$	0.58(10)	18.6°	0.041
2.82	2	$3/2^{+}$, $5/2^{+}$	2.86(12)	18.3°	0.18
3.02	2	$3/2^{+}$, $5/2^{+}$	1.80(8)	17.5°	0.12
3.23	(0 & 2)	$1/2^{+}$ & $3/2^{+}$, $5/2^{+}$	0.41(6)	16.4°	0.13 & 0.004, 0.003

a wide range of targets is consistent with the magnitude of the quenching of spectroscopic strength by short-range high-momentum correlations between nucleons [46].

Comparisons for the helium-induced reactions are also favorable, albeit at the 10% to 15% level; the comparison is not quite as good as for the (d,p) reaction, perhaps due to the use of fixed potentials in this case rather than global sets. Values of 0.48(2) and 0.47(5) have been deduced for the (α,^{3}He) [3] and (^{3}He,α) [45] reactions respectively on the stable $N = 82$ targets and 0.47(6) for the nickel isotopes [43].

The value of the normalization does depend on the choices made in the reaction modeling; a variation of ∼40% was found when different potentials were used. However, the variation in the resulting relative spectroscopic factors was only ∼15%.

TABLE V. DWBA normalizations extracted using similar techniques from independent data sets (see text for details).

Targets	Reaction	Normalization	Reference
$N = 50$	(d,p)	0.63(2)	Current work
$N = 82$	(p,d)	0.58(2)	[45]
$Z = 28$	$(d,p)/(p,d)$	0.64(5)	[43]
$N = 50$	(α,^{3}He)	0.55(1)	Current work
$N = 82$	(α,^{3}He)	0.48(2)	[3]
$N = 82$	(^{3}He, α)	0.47(5)	[45]
$Z = 28$	(α,^{3}He)	0.47(6)	[43]

The spectroscopic factors normalized according to the procedure described above are listed in Tables I, II, III, and IV.

V. DISCUSSION

The energy centroids of the observed single-particle strength corresponding to different ℓ values is summarized in Table VI, with the $\ell = 2$ strength listed separately for $J^{\pi} = 3/2^{+}$ and $5/2^{+}$ on the basis described above. In the cases where there is little unobserved low-lying strength ($\ell = 0$, 2, and 4), the variation in the observed centroids reflects changes in the underlying single-particle energy. Recent theoretical approaches have attempted to understand such shifts in orbital energies in terms of the changing effect of valence proton-neutron interactions as the neutron excess varies across the chain of nuclei and a similar approach is adopted here.

Proton occupancies in $N = 51$ are available from the results of previous measurement of proton transfer reactions [47–52] and these are summarized in Fig. 11(a). The general picture is that below $Z = 40$, the population of the $\pi g_{9/2}$ orbital is low as expected, with protons filling the $\pi p_{1/2}$, $\pi p_{3/2}$, and $\pi f_{5/2}$ orbitals. The $\pi g_{9/2}$ occupancy increases dramatically for $Z > 40$. The change from filling of a mixture of lower spin $j_{>}$ and $j_{<}$ proton orbitals below $Z = 40$, to filling a single higher spin $j_{>}$ orbital above, is likely to be reflected in the systematics of the valence neutron orbitals in these systems.

In order to investigate these trends further, calculations of effective single neutron energies were performed using a two-body force composed of a central term of Gaussian form and a tensor interaction derived from π and ρ meson exchange according to the prescription set out in Ref. [6]. For illustrative purposes, the calculations were also performed with the contribution from central forces only. The experimental proton occupancies were used for $Z \leqslant 40$; additional protons were assumed to occupy the $\pi g_{9/2}$ orbital. The results are shown in Figs. 11(b) and 11(c) compared to the experimental data.

The calculated difference between the effective single-neutron energies for the $\nu g_{7/2}$ orbital and the $\nu s_{1/2}$ orbital is shown in Fig. 11(b), both with and without the tensor contributions. These data facilitate the comparison with the current experimental data since the majority of $\ell = 4$ and

TABLE VI. Centroids of the observed single-particle strength in units of MeV. For $\ell = 0$ and 2, data is taken from the (d,p) reaction and and, for $\ell = 4$ and 5, from the (α,^{3}He) reaction, apart from ^{87}Kr where only the former reaction is available. See text for discussion of $\ell = 2$ spin assignments.

	^{87}Kr	^{89}Sr	^{91}Zr	^{93}Mo
$\ell = 0$	1.091(120)	1.325(5)	1.534(4)	1.684(6)
$\ell = 2$, $J^{\pi} = 3/2^{+}$	2.212(16)	2.257(5)	2.646(4)	2.428(12)
$\ell = 2$, $J^{\pi} = 5/2^{+}$	0.000(8)	0.434(10)	0.126(4)	0.217(6)
$\ell = 4$	2.520(4)	3.050(13)	3.018(28)	2.427(20)
$\ell = 5$[a]	2.250(2)	2.327(23)	2.189(2)	2.430(5)

[a]There is unobserved strength for $\ell = 5$ transitions.

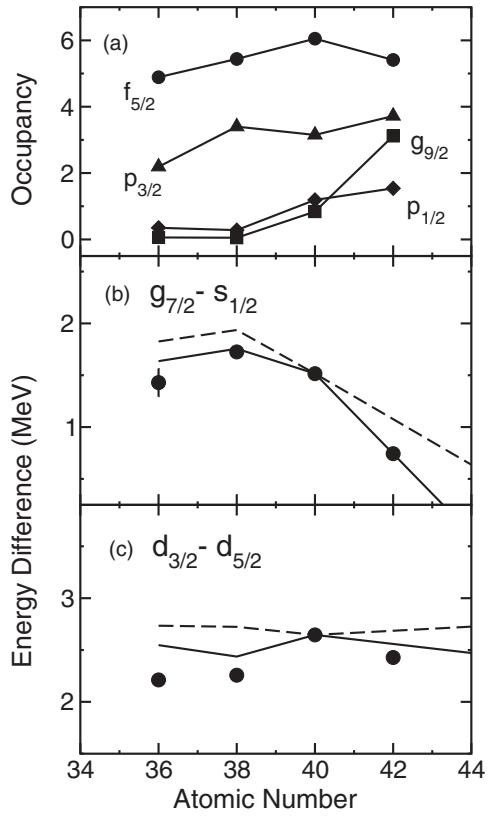

FIG. 11. (a) The proton occupancy of valence orbitals across the stable $N = 50$ isotopes taken from data in Ref. [47–52]. Measured energy differences deduced from the current work between (b) the $\nu g_{7/2}$ orbital and the $\nu s_{1/2}$ orbital, and (c) the $\nu d_{3/2}$ orbital and the $\nu d_{5/2}$ orbital. In (b) and (c), the lines are the results of calculations performed using the method presented in Ref. [6]. The solid lines include central and tensor contributions, whereas the dashed lines are results using only central forces. The theoretical predictions are anchored to the data at $Z = 40$.

$\ell = 0$ strengths have been observed and the j assignments, although model dependent, are on a relatively firm basis. The corresponding experimental data are also shown in the figure. Below $Z = 40$ with protons filling the fp shell, the radial overlaps with the $\nu g_{7/2}$ wave function are relatively small, resulting in a small variation in the $\nu g_{7/2}$ energy with Z. Once protons begin to fill the $\pi g_{9/2}$ level, there is a strong radial overlap with $\nu g_{7/2}$ neutrons; this results in increased binding arising from the contributions of central forces between protons and neutrons as indicated by the dashed line in Fig. 11(b). In addition, the tensor contribution is also attractive, as expected from the opposing sense of the spin-orbit coupling in these two single-particle states, reinforcing the additional binding. These calculations appear to describe the trends observed in the data fairly well and the reduction in the $\nu g_{7/2}$-$\nu s_{1/2}$ energy difference beyond $Z = 40$ is apparent in the data; the inclusion of the tensor effects improves somewhat the reproduction of the observed slope as the $\pi g_{9/2}$ orbitals gains occupancy.

Figure 11(c) shows the energy difference between the $\nu d_{3/2}$ and the $\nu d_{5/2}$ orbitals. The detailed correspondence between data and calculation is not as good here; this is likely to reflect the inadequacies in the assumption concerning the J assignments of $\ell = 2$ transitions. However, even with the adopted assumption, the rather constant energy across the $N = 51$ isotopes appears to follow the general picture provided by results of theoretical calculations and there is no strong evolution in the relative single-particle energies. The poor radial overlap between proton and neutron orbits tempers the interactions between them and leaves a somewhat similar change in binding energy for the two orbitals.

To summarize, the (d,p) and $(\alpha,{}^3\mathrm{He})$ reactions were studied on ^{88}Sr, ^{90}Zr, and ^{92}Mo targets. Absolute cross sections were measured, ℓ assignments made, and relative spectroscopic factors extracted. These measurements were supplemented by the $^2\mathrm{H}(^{86}\mathrm{Kr},p)^{87}\mathrm{Kr}$ measurement in inverse kinematics using the HELIOS spectrometer. The resulting observed single-particle centroids appear consistent with predictions of monopole shifts arising from central and tensor forces with changing neutron excess. The cross section data from these experiments are available online at the Experimental Unevaluated Nuclear Data List (XUNDL) database [53].

ACKNOWLEDGMENTS

This work was supported by the UK Science and Technology Facilities Council, the US Department of Energy, Office of Nuclear Physics, under Contract No. DE-AC02-06CH11357 and Grants No. DE-FG02-04ER41320 and No. DEFG02-91ER40609, and the National Science Foundation Grant No. PHY-08022648 (JINA).

[1] A. Ozawa, T. Kobayashi, T. Suzuki, K. Yoshida, and I. Tanihata, Phys. Rev. Lett. **84**, 5493 (2000).
[2] J. P. Schiffer *et al.*, Phys. Rev. Lett. **92**, 162501 (2004).
[3] B. P. Kay, S. J. Freeman, J. P. Schiffer, J. A. Clark, C. Deibel, A. Heinz, A. Parikh, and C. Wrede, Phys. Lett. B **658**, 216 (2008).
[4] B. P. Kay, J. P. Schiffer, S. J. Freeman, C. R. Hoffman, B. B. Back, S. I. Baker, S. Bedoor, T. Bloxham, J. A. Clark, C. M. Deibel, A. M. Howard, J. C. Lighthall, S. T. Marley, K. E. Rehm, D. K. Sharp, D. V. Shetty, J. S. Thomas, and A. H. Wuosmaa, Phys. Rev. C **84**, 024325 (2011).
[5] T. Otsuka, T. Suzuki, R. Fujimoto, H. Grawe, and Y. Akaishi, Phys. Rev. Lett. **95**, 232502 (2005).
[6] T. Otsuka, T. Suzuki, M. Honma, Y. Utsuno, N. Tsunoda, K. Tsukiyama, and M. Hjorth-Jensen, Phys. Rev. Lett. **104**, 012501 (2010).
[7] E. R. Cosman, H. A. Enge, and A. Sperduto, Phys. Rev. **165**, 1175 (1968).
[8] D. C. Slater, E. R. Cosman, and D. J. Pullen, Nucl. Phys. A **206**, 433 (1973).
[9] H. Blok, W. Zimmerman, J. Kraushaar, and P. Batay-Csorba, Nucl. Phys. A **287**, 156 (1977).
[10] T. P. Cleary, Nucl. Phys. A **301**, 317 (1978).

[11] H. P. Block, L. Hulstman, E. Kaptein, and J. Blok, Nucl. Phys. A **273**, 142 (1976).
[12] R. D. Rathmell, P. J. Bjorkholm, and W. Haeberli, Nucl. Phys. A **206**, 459 (1973).
[13] A. Graue, L. H. Herland, K. J. Lervik, J. T. Nesse, and E. R. Cosman, Nucl. Phys. A **187**, 141 (1972).
[14] J. B. Moorhead and R. A. Moyer, Phys. Rev. **184**, 1205 (1969).
[15] S. A. Hjorth and B. L. Cohen, Phys. Rev. **135**, B920 (1964).
[16] A. Yen, F. Ajzenberg-Selove, and B. Rosner, Nucl. Phys. A **111**, 100 (1968).
[17] W. Booth, S. M. Dalgliesh, K. C. McLean, R. N. Glover, and F. R. Hudson, Phys. Lett. B **30**, 335 (1969).
[18] C. R. Bingham and M. L. Halbert, Phys. Rev. C **2**, 2297 (1970).
[19] M. S. Zisman *et al.*, Phys. Rev. C **8**, 1866 (1973).
[20] K. Haravu, C. L. Hollas, P. J. Riley, and W. R. Coker, Phys. Rev. C **1**, 938 (1970).
[21] R. E. Sass, B. Rosner, and E. J. Schneid, Phys. Rev. **138**, B399 (1965).
[22] A. H. Wuosmaa, J. P. Schiffer, B. B. Back and C. J. Lister and K. E. Rehm, Nucl. Instrum. Methods Phys. Res. A **580**, 1290 (2007).
[23] J. C. Lighthall *et al.*, Nucl. Instrum. Methods Phys. Res. A **622**, 97 (2010).
[24] B. Singh, Nucl. Data Sheets **85**, 1 (1998) and references therein.
[25] C. M. Baglin, Nucl. Data Sheets **86**, 1 (1999) and references therein.
[26] C. M. Baglin, Nucl. Data Sheets **112**, 1163 (2011) and references therein.
[27] M. H. Macfarlane and S. C. Pieper, Argonne National Laboratory Report No. ANL-76-11 Rev. 1, 1978 (unpublished).
[28] G. Bassani and J. Picard, Nucl. Phys. A **131**, 653 (1969).
[29] E. R. Flynn, R. E. Brown, F. Ajzenberg-Selove, and J. A. Cizewski, Phys. Rev. C **28**, 575 (1983).
[30] C. M. Perey and F. G. Perey, Phys. Rev. **132**, 755 (1963).
[31] F. D. Becchetti and G. W. Greenlees, Phys. Rev. **182**, 1190 (1969).
[32] R. V. Reid Jr, Ann. Phys. (NY) **50**, 411 (1968).
[33] K. S. Low and T. Tamura, Phys. Rev. C **11**, 789 (1975).
[34] W. C. Parkinson, D. L. Hendrie, H. H. Duhm, J. Mahoney, J. Saundinos, and G. R. Satchler, Phys. Rev. **178**, 1976 (1969).
[35] J. M. Lohr and W. Haeberli, Nucl. Phys. A **232**, 381 (1974).
[36] S. S. Ipson, W. Booth, and J. G. B. Haigh, Nucl. Phys. A **206**, 3114 (1973).
[37] H. An and C. Cai, Phys. Rev. C **73**, 054605 (2006).
[38] J. J. H. Menet, E. E. Gross, J. J. Malanify, and A. Zucker, Phys. Rev. C **4**, 1114 (1971).
[39] F. G. Perey, Phys. Rev. **131**, 745 (1963).
[40] S. Galés, E. Hourani, S. Fortier, H. Laurent, J. M. Maison and J. P. Schapira, Nucl. Phys. A **288**, 221 (1977).
[41] S. S. Glickstein and G. Tessler, Phys. Rev. C **10**, 173 (1974).
[42] R. G. Helmer, Nucl. Data Sheets **95**, 543 (2002).
[43] J. P. Schiffer, C. R. Hoffman, B. P. Kay, J. A. Clark, C. M. Deibel, S. J. Freeman, A. M. Howard, A. J. Mitchell, P. D. Parker, D. K. Sharp, and J. S. Thomas, Phys. Rev. Lett. **108**, 022501 (2012).
[44] M. H. Macfarlane and J. B. French, Rev. Mod. Phys. **32**, 567 (1960).
[45] A. M. Howard, Ph.D. thesis, The University of Manchester, 2010 (unpublished).
[46] G. J. Kramer, H. P. Blok, and L. Lapikàs, Nucl. Phys. A **679**, 297 (2001).
[47] A. Pfeiffer *et al.*, Nucl. Phys. A **455**, 381 (1986).
[48] E. C. May and S. A. Lewis, Phys. Rev. C **5**, 117 (1972).
[49] L. R. Medsker, H. T. Fortune, S. C. Headley, and J. N. Bishop, Phys. Rev. C **12**, 1516 (1975).
[50] J. Harrison and S. Hiebert, Nucl. Phys. A **185**, 385 (1972).
[51] J. L. Horton and C. E. Hollandsworth, Phys. Rev. C **13**, 2212 (1976).
[52] P. Li *et al.*, Nucl. Phys. A **469**, 393 (1987).
[53] http://www.nndc.bnl.gov/xundl.